www.cadanda.com
Computer-Aided Design AND APPLICATIONS

# Determination of Elbow Flexion-Extension Axis Based on Planar and Closed B-Splines

Kamal Mostafavi[1], O. Remus Tutunea-Fatan[2],
Emily Lalone[3], Graham J. W. King[4] and James A. Johnson[5]

[1]The University of Western Ontario, smostaf2@uwo.ca
[2]The University of Western Ontario, rtutunea@eng.uwo.ca
[3]The University of Western Ontario, elalone@uwo.ca
[4]The University of Western Ontario, Graham.King@sjhc.london.on.ca
[5]The University of Western Ontario, Jim.Johnson@sjhc.london.on.ca

## ABSTRACT

Accurate determination of the flexion-extension axis of the elbow affects the outcome of implant replacement. The current study proposes an automated approach capable of determining the FE axis based on a stack of axial computer tomographic (CT) imaging slices of the distal humerus. The core of the algorithm consists of an original technique employing control polygon deformation used to approximate the segmented outer cortical bone points with closed B-Splines, followed by curvature-based and least squares fitting methods for determination of the two relevant geometric centers. The new approach was validated against a conventional voxel-based FE axis determination procedure involving marching cubes algorithm.

**Keywords:** elbow flexion-extension axis, distal humerus, voxel-based representations.
**DOI:** 10.3722/cadaps.2013.551-565

## 1 INTRODUCTION

Among human body joints, elbow is generally regarded as the articulation with the most complex anatomy. The role of the elbow within the complex kinematics and dynamics of the upper limb is often more prominent than that of the wrist and shoulder. As such, any impairments of its functionality, caused either by accidents or by various pathological conditions (fractures, arthritis, bone tumors, etc.) have to be addressed promptly.

One of common surgical procedures aiming to restore much of the lost functionality of middle articulation of the upper extremity is total elbow arthroplasty. Within the scope of this procedure, the damaged elbow articulation is partially or totally replaced by an artificial prosthetic device attempting

to match its native equivalent. One of the main factors contributing to the successful long term outcome of the surgical arthroplastic procedure is related to the accurate replication of the primary rotational axis of the elbow [13], commonly termed flexion-extension (FE) axis. Indeed, the misalignment between native and artificial FE axes alters elbow kinematics and eventually leads to implant failures, whose avoidance is highly desirable from both patient and health care economics perspectives [20].

In conventional biomechanics, the FE axis is somewhat axiomatically defined as the line that connects the centers of a spherical-like and circular-like feature which are easily identifiable on the anatomy of the distal humerus and are termed capitellum and trochlear sulcus, respectively (Fig. 1). Historically, one of the first studies to characterize the direction of FE axis belongs to [17] who showed that the elbow rotates as a uniaxial joint. London proposed to define its rotational axis as the line passing through the centers of the arcs outlined by the bottom of the trochlear sulcus and the periphery of the capitellum. Further attempts to determine the location of the FE axis were performed *in vitro* by [25] who used milled slices of cadaveric humeral specimens to obtain points along the line connecting the proposed geometric centers. While the development of modern electromagnetic and radiostereometric devices allow "online" *in vivo* determinations of the perhaps variable FE axis posture (*i.e.* position and orientation) [26,11], these methods rely heavily on the accuracy of the equipment used and are relatively difficult to instrument in a clinical setting.

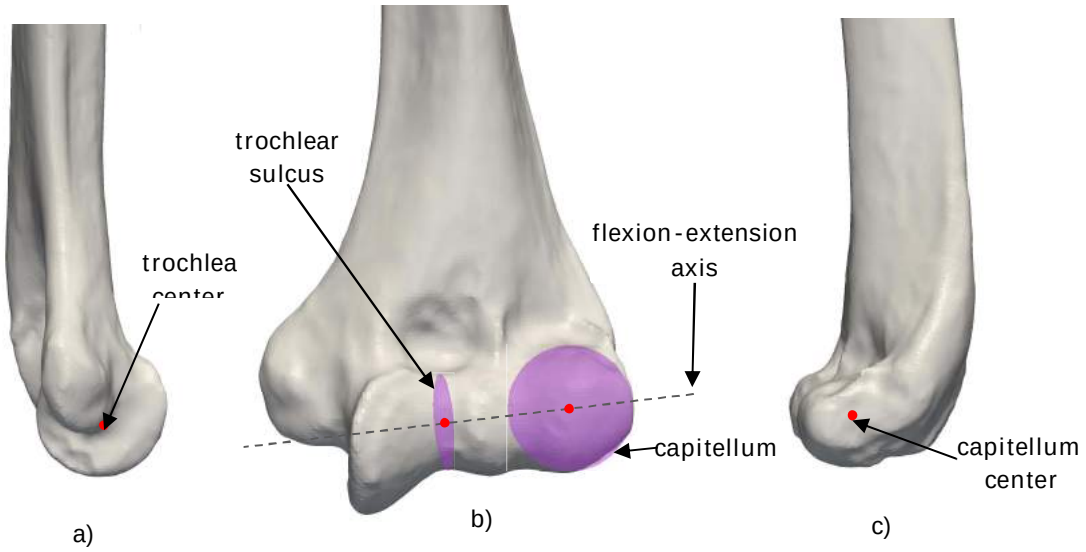


Fig. 1: Anatomical position and orientation of the flexion-extension axis: a) medial, b) anterior, and c) lateral views of the distal humerus.

Since accurate determination of the FE axis is of paramount importance during the elbow replacement procedure, surgeons are generally required to establish intereoperatively its position based on alternate humeral bony landmarks that are exposed and thereby visible during surgery [21]. However, the inherent subjectivity of this approach makes it susceptible for generation of clinically significant implant alignment errors [8].

A different approach for FE axis determination relies on the use of alternate methods to reconstruct the shape of the distal humerus, followed by geometry-specific techniques to locate the position of the two relevant centers. While simple quasi-lateral radiographic images could be sufficient

to establish the position of the two anatomical landmarks [7], other types of digital data would also be suitable for more precise and in-depth analyses of the FE axis posture. One of the first ideas in this regard was to digitize the anatomy of the capitellum and trochlea by means of a contact-based stylus, followed by the use of least-square fitting method to determine the corresponding geometric centers [16,10]. However, since this approach is only possible in context of *in vitro* studies, its later enhancements relied on CT-acquired data [9,19,20]. One of the major advantages of the **ò**offline**ó** imaging-based methods is that after the incipient *in vitro* development and validation, they can be subsequenly extended to patients by means of conventional fiducial-based registration procedures [19]. On the other hand, since in this case user interaction along with manual manipulation of the data is required, it is relatively difficult to preserve the consistency of the results among users with undesirable consequences on FE axis posture accuracy.

To address this issue, automated shape recognition methods based on imaging techniques could be employed [22], especially when combined with appropriate orientation estimation techniques that are specifically oriented towards anatomical structures [5]. However, when it comes to practical engineering applications, the effectiveness of voxel-originated representations **ð** regardless if surface or volume-based - that are omnipresent in medical imaging is at least questionable for at least two reasons [2,14]. On one hand, the accuracy of voxel-originated data is direct proportional with its overall size. Moreover, its accuracy is inherently limited by the initial size of the pixel/voxel used during body scan procedure that in turn cannot be decreased too much due to patient radiation overexposure concerns. Because of this, while the advancements in computer graphics might be arguably capable to keep up with the data volume requirements, resolution restrictions are unavoidable. Secondly, the use of the pixel/voxel-originated data within the wide range engineering applications available is impossible, since many of them require parametric (B-Spline/NURBS) data formats in order to make full use of their capabilities.

Numerous attempts were made to develop heterogeneous parametric representation of various human body external or internal elements/organs [6]. In most studies, parametric models were generated through specialized reverse engineering operations performed on data acquired via CT or MRI scans. Very often, the reconstruction of the human anatomical features comes down to approximation of the planar segmented point datasets with parametric curves determined by means of custom-written routines [3,14] or commercial CAD software [1].

The survey of the available literature reveals that in relatively rare instances the precision of the parametric models of the human body-originated shapes was checked either against their physical correspondent or against alternate imaging-based methods. Within the scope of the current study, an automated technique was developed to establish the orientation of the elbow FE axis based on the parametric models of the distal humerus. The position of the two geometric centers involved in FE axis determination was tested against a conventional method involving medical imaging-specific data and procedures. More details about the developed FE axis determination technique will be provided in the subsequent sections.

## 2 B-SPLINE BASED DETERMINATION OF FLEXION-EXTENSION AXIS

In order to determine the location of the two geometric centers that are determinant for the direction of the elbow FE axis, the first task to be accomplished is generation of a parametric representation of the distal humerus based on an input consisting of axial slices of the bone acquired through CT scanning.

### 2.1 Detection of Outer Cortical Bone Contours

The method used in this study to extract the outer contours of the cortical bone represents a direct derivation of the concept proposed by [15], according to which an accurate threshold for geometric segmentation purposes has to be set at 49% of the difference of the density between the adjacent tissues. It is important to outline here that when CT data is acquired with low power **ð** which is generally the case in clinical settings **ð** the resulting images are blurred and this has a significant impact on the dimensional precision of the segmented bone contours. Specifically, when segmentation threshold value is set too high, the resulting representation of the bone will be smaller than its physical correspondent, whereas when threshold value is set too low, CT bone model will yield larger than the actual object.

The thresholding technique used in this study was based on the percentage of the brightest pixel identified in each of the CT slices analyzed. After performing a series of preliminary tests involving outer bone contour segmentation with various thresholds, followed by verification against the scanned humeral specimen, it was established that the best dimensional match between digital and physical representations of the bone is achieved when 40% from the brightest pixel intensity is used as a cutoff value. By employing this threshold value, the segmentation algorithm zigzagged through the columns of the 2D matrix of pixels characteristic to each CT slice and retained the row of the first and last pixel of each column satisfying the set thresholding condition. Obviously, no pixels were extracted for columns placed away from bone cross sectional area (Fig. 2a).

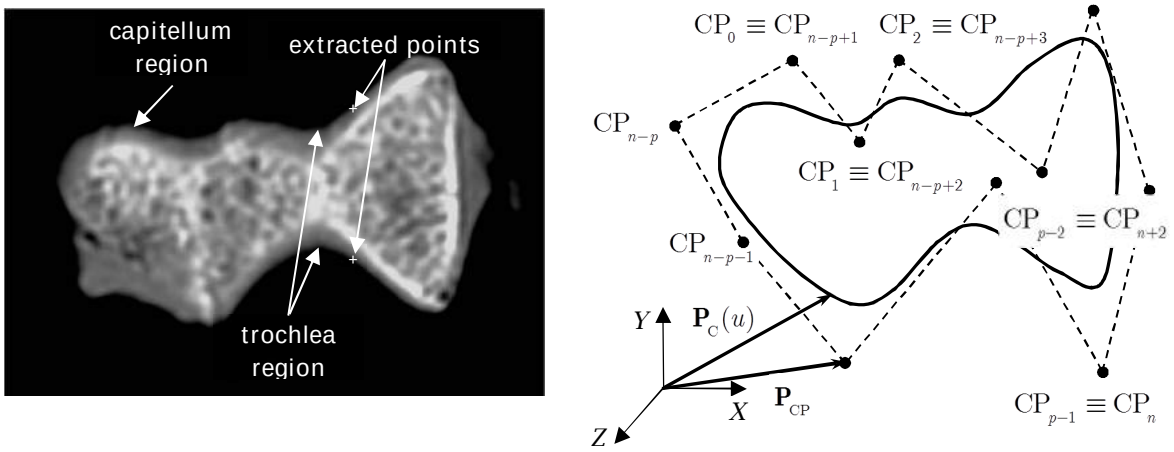


(a) (b)

Fig. 2: Representative axial cross sections through distal humerus: (a) raw CT slices, and (b) parametric curve-approximated outer bone contours.

Furthermore, the characteristics of the scanning (column zig-zag and horizontal left-right) process performed on the 2D matrix of pixels ensure that segmented CT data points form an array that can be easily ordered based on their $X$ (or $Y$) coordinates, such that geometrically adjacent/neighboring points become consecutively placed in the array. This sequentiality bears a particular importance from the perspective of the curve fitting technique to be detailed below.

### 2.2 Planar and Closed B-Spline Fitting by Control Polygon Deformation

Given the level of maturity acquired by the parametric representations in context of engineering applications, this type of curves was chosen to approximate the point dataset extracted through the

thresholding technique outlined at Section 2.1. Furthermore, among the existing pool of parametric curves, planar and closed B-Splines are deemed to be capable to trace the outer contours of distal humerus with sufficient precision. Both planar and closed characteristics of the parametric curves used are dictated by the intrinsic features of the acquired CT slices and humeral cross sections, respectively.

According to generic computer-aided geometric modeling theory, the parametric form of planar and closed B-Splines (Fig. 2b) is:

$$\mathbf{P}_{\mathrm{B}}(u)=\sum_{i=0}^{n}N_{i,k}(u)\cdot\mathbf{P}_{\mathrm{CP}_i} \tag{1}$$

where $\mathbf{P}_{\mathrm{CP}_i}=\begin{Bmatrix}X_{\mathrm{CP}_i}\\Y_{\mathrm{CP}_i}\\Z_{\mathrm{CP}_i}\end{Bmatrix}$ are the $n+1$ vertices of the control polygon, and $u\in[u_p,u_{n+1}]$ is the inherent parameter of the curve. In Eq. (1) $k=p+1$ represents the order of the $p$-th degree curve. The present study relied on the control point wrapping technique to generate the parametric expression of closed and planar ($Z_{\mathrm{CP}_i}$ = const.) B-Splines as described by [4]. According to this method, the last $p$ points are to coincide with the first $p$ points of the control polygon in order to close an initially open B-Spline:

$$\mathbf{P}_{\mathrm{CP}_i}=\mathbf{P}_{\mathrm{CP}_{n-p+1+i}},\text{for}\,i\in\{0,1,\ldots,(p-1)\} \tag{2}$$

The closed form of the curve implies that

$$\mathbf{P}_{\mathrm{B}}(u_p)=\mathbf{P}_{\mathrm{B}}(u_{n+1}) \tag{3}$$

The $N_{i,k}(u)$ parametric functions used to blend the influence of $n+1$ control points $\mathbf{P}_{\mathrm{CP}_i}$ in Eq. (1) are defined by the well known Cox-de Boor recursive formula:

$$\begin{aligned}&N_{i,j}(u)=\frac{u-u_i}{u_{i+j}-u_i}N_{i,j-1}(u)+\frac{u_{i+j+1}-u}{u_{i+j+1}-u_{i+1}}N_{i+1,j-1}(u)\\&\text{for}\,j\in\{0,1,\ldots,k\}\,\text{and}\,i\in\{0,1,\ldots,(n+k-j-1)\}\end{aligned} \tag{4}$$

with initial conditions set by:

$$\begin{aligned}&N_{i,1}(u)=\begin{cases}1,\text{if}\,u\in[u_i,u_{i+1}),\text{for}\,i\in\{0,1,\ldots,(n+k-2)\}\\0,\text{otherwise}\end{cases}\\&\frac{0}{0}=0\end{aligned} \tag{5}$$

It is important to emphasize here that while the total length of the knot vector $\mathbf{U}=\{u_0\quad u_1\quad\ldots\quad u_m\}$ of the cubic B-Spline curve is $m=n+k+1$, the active range of its closed form is defined only

between $u_p$ and $u_{n+1}$, to a total of $m-2p$ knots. The planar and closed B-Splines built on these theoretical premises are $C^{p-1}$ continuous.

When it comes to the actual determination of knot values, numerous attempts were made to propose robust parametrization schemes capable to trace even highly sparse and/or unevenly distributed datapoints. While the number of studies focused on determination of adequate parametrizations for closed B-Spline is considerably smaller, some progress in this direction was also reported in the literature [23]. Within the limited scope of the current study, and by taking into consideration the relative uniformity and density of the datapoints to be approximated by the closed B-Spline, just uniform parametrization was tested:

$$u_{i+1} = u_i + 1, \text{for } i \in \{p,(p+1),...,n\} \tag{6}$$

Based mathematical formulation outlined by Eqs. (1-7) above, planar and closed B-Spline curves are fully determined once their control polygon and knot vector are known. Because of this, the current problem at hand comes down eventually to the development of a robust B-Spline fitting technique, capable to approximate with a certain tolerance/accuracy a given of extracted data points. Many of the presently available solutions in this regard rely or are derived ðto a larger or a lesser extent ð on the knot removal techniques as originally detailed by [24] in their comprehensive monograph on NURBS. Nevertheless, the current work employed a completely different approach, essentially inspired from a recent observation according to which a ògoodó B-Spline would not deviate much from its control polygon [12].

The novel approach developed in the framework of the present study for B-Spline fitting purposes is based on a knot insertion technique performed to support a deforming control polygon whose length increases progressively to enable a superior approximation of the given datapoints. The continuous reshaping of the closed B-Spline is controlled at two different levels, via global and local tolerances, respectively. To satisfy this condition, global control $\varepsilon_{\text{mean}}$ is defined as a mean deviation of all given CT data points $\mathrm{D}_i$ to the closed B-Spline curve:

$$\varepsilon_{\text{mean}} = \frac{1}{n_{\text{D}}} \cdot \sum_{i=0}^{n_{\text{D}}} |\mathbf{P}_{\text{D}_i} - \underset{\text{B}}{\text{proj}}(\mathbf{P}_{\text{D}_i})| \tag{7}$$

where $n_{\text{D}}$ represents the number of extracted CT data points, and $\underset{\text{B}}{\text{proj}}(\mathbf{P}_{\text{D}_i})$ represents the location of the projection (footprint) of $\mathrm{D}_i$ on the closed B-Spline curve. For each analyzed data point, the projection is determined through a nonlinear bounded optimization technique employing golden section search and parabolic interpolation while seeking for the point on the curve whose normal passes through $\mathrm{D}_i$. As expected, $|\mathbf{P}|$ in Eq. (7) represents the Euclidian norm of the three-dimensional vector $\mathbf{P}$.

In addition to $\varepsilon_{\text{mean}}$, a local control was also used:

$$\varepsilon_{\text{max}} = \max_{i \in \{0,...,n_{\text{D}}\}} (|\mathbf{P}_{\text{D}_i} - \underset{\text{B}}{\text{proj}}(\mathbf{P}_{\text{D}_i})|) \tag{8}$$

The core of the developed curve fitting algorithm consists in the iterative addition of new control points that are selected in a manner capable to gradually reduce the distance between given dataset and approximating curve. Following Floaterõs idea [12], control points are in fact intentionally chosen to be a subset of the data points to be approximated ($\mathrm{CP}_i \in \{\mathrm{D}_0, \mathrm{D}_1, ..., \mathrm{D}_{n_{\text{D}}}\}$). Due to the particularities

of the CT thresholding method used, each control point of the approximating B-Spline can be uniquely identified within the initial array of given data points ($\mathrm{CP}_i \equiv \mathrm{D}_{\mathrm{CP}_i} \equiv \mathrm{D}_l$).

The algorithm used to fit a closed and planar cubic B-Spline to the segmented points of the distal humerus consists of the three major steps:

*Step 1: Initialization.*

The algorithm starts off by generating a closed B-Spline whose shape is determined by the location of four control points selected in extreme positions with respect to the initial dataset of segmented CT points (Fig. 3a):

$$\begin{aligned}
\mathbf{P}_{\mathrm{CP}_0} &= \mathbf{P}_{\mathrm{D}_i} \Big| X_{\mathrm{D}_i} = \min_{j\in\{0,\ldots,n_{\mathrm{D}}\}} (X_{\mathrm{D}_j}) \\
\mathbf{P}_{\mathrm{CP}_1} &= \mathbf{P}_{\mathrm{D}_i} \Big| X_{\mathrm{D}_i} = \max_{j\in\{0,\ldots,n_{\mathrm{D}}\}} (Y_{\mathrm{D}_j}) \\
\mathbf{P}_{\mathrm{CP}_2} &= \mathbf{P}_{\mathrm{D}_i} \Big| Y_{\mathrm{D}_i} = \max_{j\in\{0,\ldots,n_{\mathrm{D}}\}} (X_{\mathrm{D}_j}) \\
\mathbf{P}_{\mathrm{CP}_3} &= \mathbf{P}_{\mathrm{D}_i} \Big| Y_{\mathrm{D}_i} = \min_{j\in\{0,\ldots,n_{\mathrm{D}}\}} (Y_{\mathrm{D}_j})
\end{aligned} \tag{9}$$

*Step 2: Global modification.*

This step ensures that the mean error defined by Eq. (7) becomes smaller than a certain predefined tolerance:

$$\varepsilon_{\mathrm{mean}} \le \Delta_{\mathrm{global}} \tag{10}$$

To achieve this goal, a new control point is dichotomically added between each pair of successive control points, such that each control point segment is practically replaced by two new ones. The new points added to the control dataset in each iteration are those located at maximum distances with respect to the current location of the control polygon segments according to the following relationship:

$$\mathbf{P}_{\mathrm{CP}_i^{\mathrm{new}}} = \mathbf{P}_{\mathrm{D}_{\max}} \Big| \, |\, \mathbf{P}_{\mathrm{D}_{\max}} - (\mathbf{P}_{\mathrm{CP}_{i+1}} - \mathbf{P}_{\mathrm{CP}_i}) \,| = \max_{j\in\{l,\ldots,(l+1)\}} (|\, \mathbf{P}_{\mathrm{D}_j} - (\mathbf{P}_{\mathrm{CP}_{i+1}} - \mathbf{P}_{\mathrm{CP}_i}) \,|) \tag{11}$$

This step iterates around the contour of the bone until global tolerance condition in Eq. (10) is satisfied. The new control point $\mathbf{P}_{\mathrm{CP}_i^{\mathrm{new}}}$ is inserted in the control point array between $\mathbf{P}_{\mathrm{CP}_i}$ and $\mathbf{P}_{\mathrm{CP}_{i+1}}$.

*Step 3: Local modification.*

Once the global condition of tolerance was met, fitting algorithm moves in the local modification stage, according to which a new preset modifier is being enforced:

$$\varepsilon_{\max} \le \Delta_{\mathrm{local}} \tag{12}$$

The maximum distance condition between given points and fitted B-Spline expressed through the definition of $\varepsilon_{\max}$ in Eq. (8) is now being checked around the entire contour of the parametric curve. A new control point is added to the dataset whenever the condition outlined by Eq. (12) is not verified. The new control point to be included for the next iterative representation of the fitted curve represents precisely the point located at the maximum distance with respect to the

$$\mathbf{P}_{\mathrm{CP}_i^{\mathrm{new}}} = \mathbf{P}_{\mathrm{D}_{\max}} \Big| \, |\, \mathbf{P}_{\mathrm{D}_{\max}} - \operatorname*{proj}_{\mathrm{B}}(\mathbf{P}_{\mathrm{D}_{\max}}) \,| = \max_{j\in\{l,\ldots,(l+1)\}} (|\, \mathbf{P}_{\mathrm{D}_j} - \operatorname*{proj}_{\mathrm{B}}(\mathbf{P}_{\mathrm{D}_j}) \,|) \tag{13}$$

Similar to the global modification phase, the new control points identified in a certain iterative step are always inserted in the control point array according to their sequential position, *i.e.* between $\mathrm{CP}_i$ and $\mathrm{CP}_{i+1}$ which correspond to $l$ and $l+1$ counters in Eq. (13), respectively. Based on the known local modification properties of the B-Spline curves, each iterative step around the closed contour performs a gradually decreasing number of control point additions until the local tolerance condition is met.

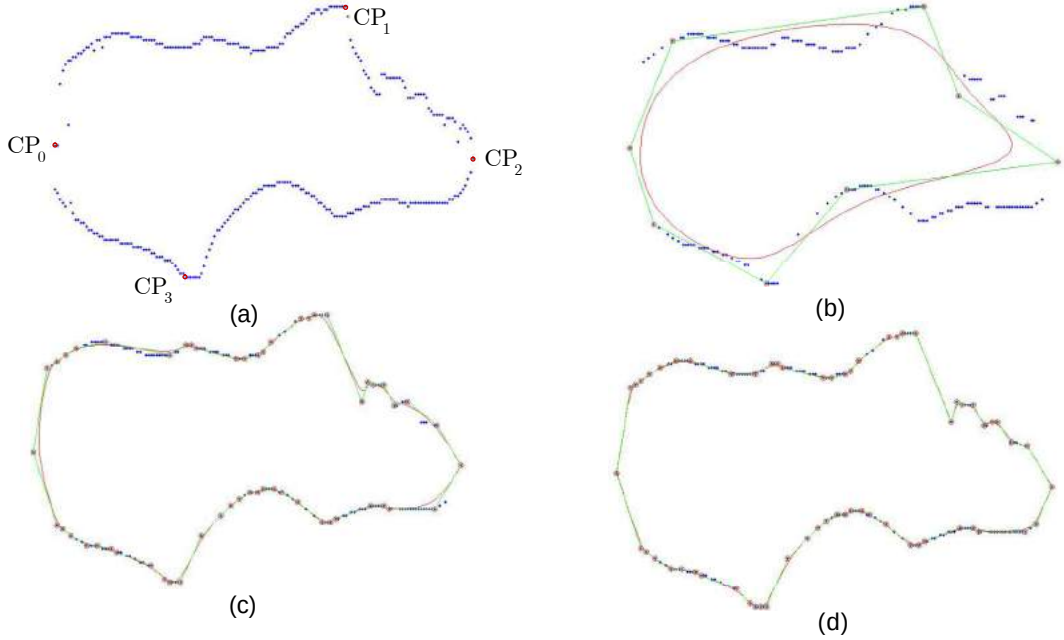


Fig. 3: Progressive adaptation of the fitted B-Spline curve shape: (a) initial set of segmented CT points, (b) approximating curve after one global modification iteration (one Step 2), (c) approximating curve at the end of the global modification phase (end of Step2), and (d) final shape of the approximating curve (end of Step 3).

The iterative application of the B-Spline fitting technique based on control polygon deformation enables a progressive wrapping of the control polygon around the extracted CT points, as depicted in Fig. 3. All decisions made during technique development phase were meant to ensure the efficiency, simplicity and precision of the proposed approach, but at the same time one of the major objectives of the novel curve fitting method was to reduce the need for subsequent B-Spline fairing/smoothing.

### 2.3 Automated Detection of Relevant Features through Local Curvature Analysis

Once the outer contours of the distal humerus were approximated with planar and closed cubic B-Splines, the next task comes down to identification of their regions with relevance in FE axis position determination. Given the fact that capitellum and trochlea regions (Fig. 2a) are involved in sphere and circle fitting respectively, a number of points have to be placed on the parametric curves in appropriate locations. In the current approach, determination of the regions of interest of the B-Splines has been performed through an in-depth analysis of their local curvature pattern. Figure 4 illustrates the variation of the local curvature along a sample B-Spline whose nonessential lateral portion was trimmed off for clarity purposes.

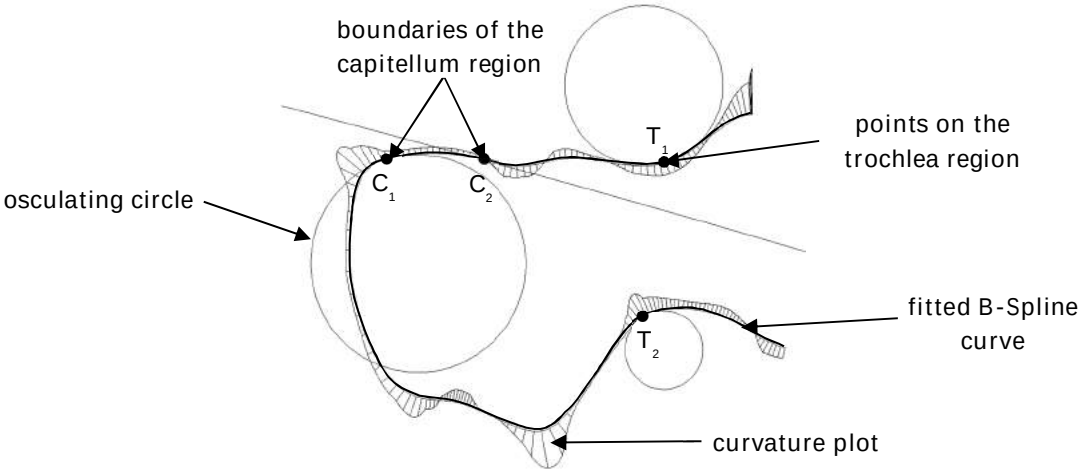


Fig. 4: Sample of local curvature pattern along distal humeral B-Splines.

As it can be observed, all significant points of the analyzed planar B-Spline slices ($\mathrm{C}_1, \mathrm{C}_2, \mathrm{T}_1, \mathrm{T}_2$) are in fact associated with major changes in the curvature variation. As such, their spatial location can be uniquely specified in conjunction with curvature-related conditions.

According to the fundamentals of differential geometry, the curvature of a parametrically-expressed planar curve can be determined with:

$$\kappa_{\mathrm{B}}(u) = \frac{\frac{dX_{\mathrm{B}}(u)}{du} \cdot \frac{d^2Y_{\mathrm{B}}(u)}{du^2} - \frac{d^2X_{\mathrm{B}}(u)}{du^2} \cdot \frac{dY_{\mathrm{B}}(u)}{du}}{\left[\left(\frac{dX_{\mathrm{B}}(u)}{du}\right)^2 + \left(\frac{dY_{\mathrm{B}}(u)}{du}\right)^2\right]^{\frac{3}{2}}} \tag{14}$$

where $X_{\mathrm{B}}(u)$ and $Y_{\mathrm{B}}(u)$ constitute the components of the general B-Spline curve defined by Eq. (1). Since this signed value can be easily calculated for each of the reconstructed B-Splines of the distal humerus, the geometric position of the four points with relevance in FE axis determination can be established based on the following criteria:

$$\begin{aligned}
&\mathbf{P}_{\mathrm{T}_1} = \mathbf{P}_{\mathrm{B}}(u_{\mathrm{T}_1}) \Big| \kappa(u_{\mathrm{T}_1}) = \max_{X_{\mathrm{T}} < X_{\mathrm{CP}_1}} (|\kappa(u_{\mathrm{T}})|) \\
&\mathbf{P}_{\mathrm{T}_2} = \mathbf{P}_{\mathrm{B}}(u_{\mathrm{T}_2}) \Big| \kappa(u_{\mathrm{T}_2}) = \max_{X_{\mathrm{T}} > X_{\mathrm{CP}_3}} (|\kappa(u_{\mathrm{T}})|) \\
&\mathbf{P}_{\mathrm{C}_{1,2}} = \mathbf{P}_{\mathrm{B}}(u_{\mathrm{C}_{1,2}}) \Big| \kappa(u_{\mathrm{C}_2}) = 0, X_{\mathrm{T}_1} > X_{\mathrm{C}_2} > X_{\mathrm{C}_1}, \underset{u \in (u_{\mathrm{C}_1}, u_{\mathrm{C}_2})}{\kappa}(u_{\mathrm{T}}) \approx \mathrm{const.}
\end{aligned} \tag{15}$$

For the two points outlining the trochlea region ($\mathrm{T}_1, \mathrm{T}_2$) as well as for one of the bounds of the capitellum region ($\mathrm{C}_2$), numerical searches based on golden section search were used to determine their corresponding parameter values ($u_{\mathrm{T}_1}, u_{\mathrm{T}_2}, u_{\mathrm{C}_2}$) along the analyzed B-Spline. These searches were facilitated by the local extremum or zero conditions outlined by Eq. (15), as well as by the particular position of these points with respect with cross sectional landmarks defined by Eq. (9), which

essentially became the initial guess points of the numerical technique. A special mention has to be made about $C_2$, which actually requires a triple pass through zero curvature condition, while the trochlea points $T_1, T_2$ were found at the first curvature extremum encountered at the left of $CP_1$ and at the right of $CP_3$, respectively. Here, the **ò**left**ó** and **ò**right**ó** directions are associated with search direction expressed in terms of parameter $u$, which decreases in both situations. Once $C_2$ was found, $C_1$ will be always located at the left end of the approximately constant curvature region of the B-Spline. This represents a direct consequence of the spherical geometry of the capitellum. Once both $u_{C_1}$ and $u_{C_2}$ are assessed, a number of discrete points are generated on the curve segment between them, to be subsequently used in the geometric feature evaluation. Minor adaptations of the search directions/boundaries in Eq. (15) are required when switching between left and right hand humeral specimens.

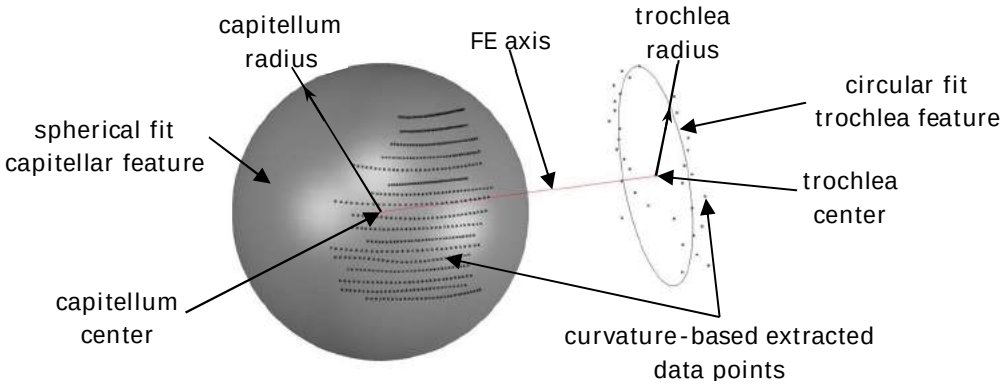


Fig. 5: Determination of the geometric characteristics of FE axis through least squares fitting.

After all relevant capitellum and trochlea points are identified and then extracted from closed B-Splines, standard least squares fitting methods based on Gauss Newton searches were employed to establish the geometric characteristics of the spherical and circular features associated with capitellum and trochear shapes (Fig. 5). The circular profile of the trochlea requires determination of its characteristic plane prior to other geometric computations. As mentioned in the introductory section, the line connecting capitellum and trochlea centers is generally acknowledged as the FE axis of the elbow articulation. In addition to their positional attributes, the fitting technique facilitates radius-based dimensional characterization of the two anatomical landmarks of interest.

## 3 CONVENTIONAL VOXEL-BASED DETERMINATION OF FE AXIS

This imaging-oriented method was used to provide a comparison basis for the original B-Spline based approach described in Section 2. The conventional technique, originally developed in a clinical study [16], was subsequently tested also in a navigated implantation and/or computer simulated context [19,20,28].

Similar to parametric geometry approach, the procedure relies on an input consisting of CT scans of the analyzed humeral specimen. Following image acquisition and thresholding/segmentation, the polygonal mesh representation of the distal humerus is generated by means of a custom-written

numerical code developed in conjunction with Visualization Toolkit graphic libraries [27]. The core of the polygonal mesh generation engine consists of marching cubes algorithm [18]. Once the humeral surface has been constructed, the user is required to roughly locate in a graphically interactive manner the capitellum and trochlea regions. This operation is performed by selecting manually nine and three points on capitellum and trochlea respectively that are capable to delimit the shape of the analyzed anatomical features (Fig. 6).

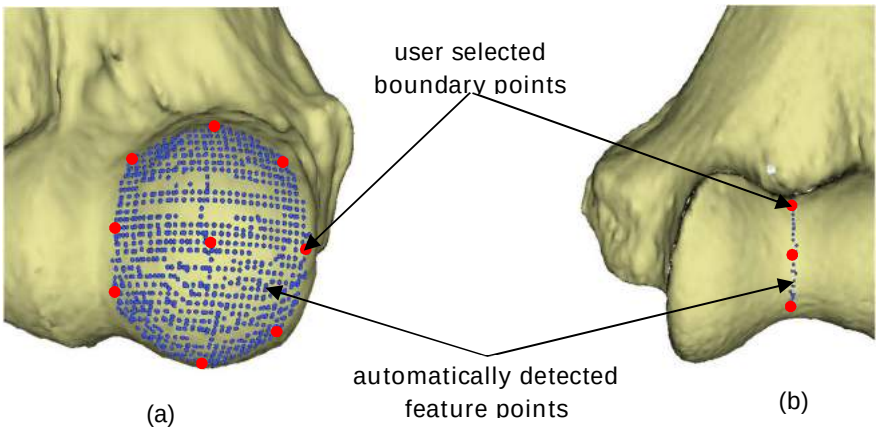


Fig. 6: Graphical localization of the anatomical features of interest through manual delimitation of their boundaries for: (a) capitellum, and (b) trochea.

Once their boundaries have been identified, the developed numerical algorithm employs a proximity search to determine all polygonal mesh vertices that are placed within the previously selected limits of the feature. Once the coordinates of all relevant points of the humerus have been found (Fig. 6), least squares method was once more used to establish the posture of the FE axis, along with dimensional characteristics of the capitellum and trochea.

## 4 RESULTS AND DISCUSSION

In order to compare the two approaches, fresh-frozen specimens of distal humerus were acquired with a 64-slice GE LightSpeed Ultra computer tomograph. The CT scans were acquired from by placing the humeral bone in a position of approximate coaxiality between its longitudinal canal (axis) and that of the CT scanner. The scanning parameters were set to approximately replicate the clinical settings with a field of view of 16x16 cm and a power of 120 kVp at 90 mAs. The stack of raw CT slices generated was characterized by a resolution of 512x512 pixels and a voxel size of 0.3125x0.3125x0.625 mm. Once the images were acquired, the position and orientation of the FE axis was determined through parametric and voxel-based techniques detailed in Sections 2 and 3, above. The two end tolerances for Steps 2 and 3 of the parametric approach were set at $\Delta_{\text{global}} = 0.2$ and $\Delta_{\text{local}} = 0.5$ respectively.

A visual comparison of the results for one of the analyzed specimens is presented in Fig. 7. As it can be noticed, the size and location of the two relevant features determined through the B-Spline approach matches reasonably well both the position of the real anatomical landmarks, as well as the set of points used to determine the FE axis through the conventional approach that will be further used as a baseline in the following quantitative comparisons.

It should be noted here that the term ‘error’ is intentionally avoided from the upcoming discussion, as it would somehow imply that a ‘golden standard’ has been used as a baseline - perhaps in the form of hard measurements performed directly on physical specimens. While this type of investigations is possible, they were simply regarded as out of the scope of the current study since they would require a more detailed understanding of the effect of environmental conditions (temperature, humidity) on the surface hardness and dimensional characteristics of the distal humerus. Because of these considerations, the conventional voxel-based approach will be treated as a reliable reference, since it was previously validated in the clinical context.

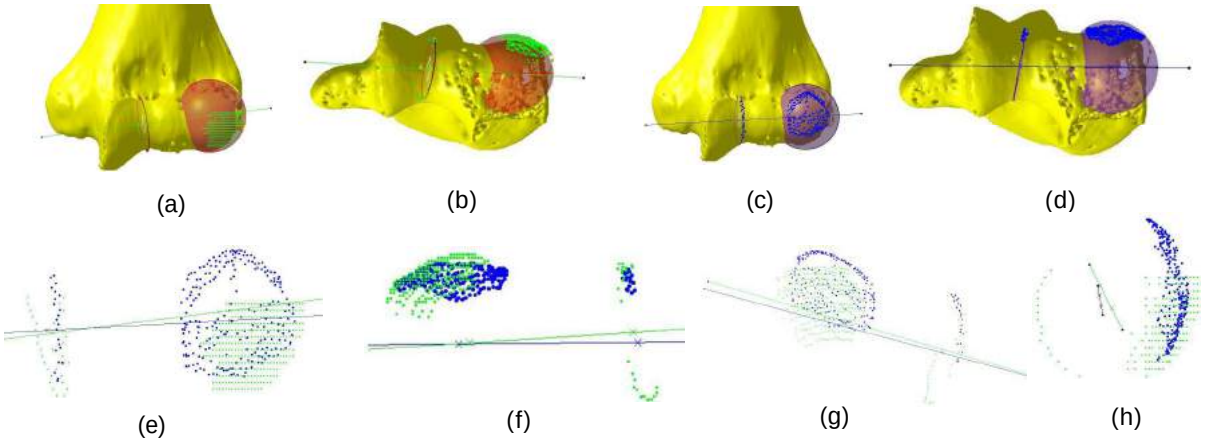


Fig. 7: Qualitative comparisons between the resulting point datasets obtained through B-Spline (green) and conventional (blue) approaches achieved through: (a)-(d) combined fitted features and bone overlay, (e)-(h) direct result overlay.

To better quantify the differences in output between the two techniques, three different specimens were processed in parallel through both methods and Tab. 1 summarizes the main geometric discrepancies between them.

| *Feature Name* | *Conventionally Determined Feature Size* | *Difference between Methods* | *Difference between Methods [%]* |
|---|---|---|---|
| Capitellum radius | 9.02 ð 11.24 mm | 0.39 ð 1.78 mm | 4.31 ð 15.83 |
| Trochlea radius | 6.95 - 8.98 mm | 0.48 - 0.76 mm | 6.94 ð 8.51 |
| FE axis length | 17.67 ð 22.03 mm | 0.34 ð 0.77 mm | 1.52 - 4.34 |
| Capitellum center location | - | 1.23 ð 3.16 mm | - |
| Trochlea center location | - | 1.35 ð 1.67 mm | - |
| FE axes misorientation | - | 4.11 ð 7.71º | - |
| Troch planes | - | 4.53 - 7.31º | - |

Tab. 1: Quantitative comparisons between B-Spline and voxel-based methods

As it can be observed, while the two techniques will yield comparable results, their output does not overlap perfectly. The numbers presented in Tab. 1 seem to imply that while a better match and consistency exists for trochlea geometry, larger variations are generally present in conjunction with

capitellar geometry. Given the inherent complexity of the two procedures presented for FE axis determination, the differences between them are somewhat expectable, especially since their only commonalities are related to the initial stack of raw CT slices and least squares fitting procedure, among which the latter one is prone to yield different results when initialized with different guess values. Among the other factors that can be deemed responsible for result variability, the differences in segmentation and outer bone surface generation techniques would most likely play a major role. The difference in thresholding parameters would explain well the consistently smaller size of the features obtained through the parametric approach. Furthermore, some supplementary inconsistencies were probably also introduced via the manual input required from the user in the conventional approach in order to delimit the two relevant anatomical features.

On the other hand, given the stability of the anatomical conformation of the distal humerus, the automated feature recognition method described in Section 2.3 can be automatically applied to different humeral specimens, since it requires a minimal input from the user. However, this pattern-oriented method assumes that: 1) the analyzed planar slices are characterized by a certain morphological consistency, and 2) the CT data was acquired in a certain orientation of the humeral specimen. While assumption 2 can be easily corrected through successive coordinate transformations, assumption 1 prevents the application of this technique in regions of the distal humerus where cross sectional slices are truncated/incomplete with respect of the standard shape shown in Fig 3. As such, the extreme top and bottom slices through capitellum and trochlea regions cannot be included in the developed parametric-based determinations of FE axis and this will cause additional result deviations. This limitation of the developed method becomes obvious in Fig. 7e and 7h, but **ð** taken alone **ð** it should not represent a major source of result mismatch, provided that the capitellum shape is indeed spherical, as assumed.

## 5 CONCLUSIONS

The present study presents a novel method capable to automatically determine the posture of elbow flexion-extension axis by starting off with a minimal input consisting of a stack of raw of CT slices of the distal humerus. A three-specimen validation of the proposed approach against a conventional voxel-based determination revealed that while their outcomes are reasonably comparable, a number of factors might cause deviations between results that could add up to 15%. However, while from a pure engineering perspective the magnitude of the discrepancies might be regarded as borderline satisfactory, the current medical practices will likely treat them as acceptable, since surgeons generally lack the adequate means to accurately position the two relevant centers during surgery. Future extensions of this work will aim the validation of the proposed methodology via physical measurements, in an attempt to improve further its inherent reliability and precision.

## ACKNOWLEDGEMENTS

This work was supported in part by Natural Sciences and Engineering Research Council of Canada (NSERC) and Canadian Institutes of Health Research (CIHR).

## REFERENCES

[1] Ameddah, H.; Assas, M.: Bio-CAD reverse engineering of free-form surfaces by planar contours, Computer-Aided Design and Applications, 8, 2011, 3-21. DOI: 10.3722/cadaps.2011.37-42

[2] Anderson, C.W.; Crawford-Hines, S.: Fast Generation of NURBS Surfaces from Polygonal Mesh Models of Human Anatomy, Technical Report CS-99-101, Colorado State University, 2000, 1-9. CiteSeerX DOI: 10.1.1.130.7533

[3] Ane, B. K.; Roller, D.: CAD Modelling in Reverse Engineering: Generating $C^2$-continuous planar B-spline curves for free-form shapes. In: Proceedings of the World Automation Congress (WAC2010), IEEE Xplore, Washington DC, USA, September 2010, ISBN: 1-889335-42-8.

[4] Alavala, C.R.: CAD/CAM Concepts and Applications, Prentice-Hall, New Delhi, 2008, 173-175.

[5] Bagci, U.; Udupa, J.-K.; Chen, X.: Orientation Estimation of Anatomical Structures in Medical Images for Object Recognition. In: Proceedings of the SPIE, 7962, 2011, 79622L-2. DOI: 10.1117/12.878184

[6] Bhatt, A.-D.; Warkhedkar, R.M.: Reverse Engineering of Human Body: A B-spline based Heterogeneous Modeling Approach, Computer-Aided Design and Applications, 5, 2008, 194-208. DOI: 10.3722/cadaps.2008.194-208

[7] Bottlang, M.; O'Rourke, M.R.; Madey, S.M.; Steyers, C.M.; Marsh, J.L.; Brown, T.D.: Radiographic Determinants of the Elbow Rotation Axis: Experimental Identification and Quantitative Validation, Journal of Orthopedic Research, 18, 2000, 821-828. DOI: 10.1002/jor.1100180521

[8] Brownhill, J.-R.; Furukawa, K.; Faber, K.-J.; Johnson, J.-A.; King, G.J.W.: Surgeon accuracy in the selection of the flexion-extension axis of the elbow: An in vitro study, Journal of Elbow and Shoulder Surgery, 15, 2006, 451-456. DOI: 10.1016/j.jse.2005.09.011

[9] Brownhill, J.R.; King, G.J.; Johnson, J.A.: Morphologic analysis of the distal humerus with special interest in elbow implant sizing and alignment, Journal of Elbow and Shoulder Surgery, 16 Suppl 2007, S126–S132. DOI: 10.1016/j.jse.2006.01.018

[10] Duck, T.R; Dunning, C.E.; Armstrong, A.D.; Johnson, J.A.; King, G.J.: Application of screw displacement axes to quantify elbow instability, Clinical Biomechanics, 18, 2003, 303–310. DOI: 10.1016/S0268-0033(03)00021-4

[11] Ericson, A.; Arndt, A.; Stark, A.; Wretenberg, P.; Lundberg, A.: Variation in the position and orientation of the elbow flexion axis, Journal of Bone and Joint Surgery, 2003, 85-B, 538–541. DOI: 10.1302/0301-620X.85B4.13925

[12] Floater, M.S.: On the deviation of a parametric cubic spline interpolant from its data polygon, 25, 2008, 148-156. DOI: 10.1016/j.cagd.2007.08.001

[13] Gramstad, G.-D.; King, G.-J.W.; O'i Driscoll, S.-W.; Yamaguchi, K.: Elbow Arthroplasty Using a Convertible Implant, Techniques in Hand and Upper Extremity Surgery, 9, 2005, 153–163.

[14] Grove, O.; Rajab, K.; Piegl, L.-A.; Lai-Yuen, S.: From CT to NURBS: Contour Fitting with B-spline Curves, Computer-Aided Design & Applications, 8, 2011, 3-21. DOI: 10.3722/cadaps.2011.3-21

[15] Hangartner, T.N.: Thresholding technique for accurate analysis of density and geometry in QCT, pQCT and µCT images, Journal of Musculoskeletal and Neuronal Interactions, 7, 2007, 9-16.

[16] King, G.-J.W.; Zarzour Z.-D.S.; Rath, D.-A.; Dunning, C.-E.; Patterson, S.-D.; Johnson, J.-A.: Metallic Radial Head Arthroplasty Improves Valgus Stability of the Elbow, Clinical Orthopedics and Related Research, 368, 1999, 114-125.

[17] London, J.T: Kinematics of the Elbow, Journal of Bone and Joint Surgery, 63-A, 1981, 529-535.

[18] Lorensen, W.E.; Cline, H.E.: Marching cubes: a high-resolution 3D surface construction algorithm. In: Proceedings of the 14th Annual Conference on Computer Graphics and Interactive Techniques (SIGGRAPH'87), 21, 163-169.

[19] McDonald, C.-P.; Beaton, B.-J. B.; King, G.-J.W.; Peters, T.-M.; Johnson, J.-A.: The effect of anatomic landmark selection of the distal humerus on registration accuracy in computer-assisted elbow surgery, Journal of Elbow and Shoulder Surgery, 17, 2008, 833-843. DOI: 10.1016/j.jse.2008.02.007

[20] McDonald, C.-P.; Johnson, J.-A.; Peters, T.-M.; King, G.-J.W.: Image-based navigation improves the positioning of the humeral component in total elbow arthroplasty, Journal of Elbow and Shoulder Surgery, 19, 2010, 533-543. DOI: 10.1016/j.jse.2009.10.010
[21] Morrey, B.F.; Hotchkiss, R.F.: External fixators of the elbow. In: The elbow and its disorders, edited by B.F. Morrey, 2000, Saunders, Philadelphia, 457ð467.
[22] Mundy, J.L.: Object Recognition in the Geometric Era: a Retrospective, 2006, 1-29. CiteSeerX DOI: 10.1.1.103.6802
[23] Park, H.: Choosing nodes and knots in closed B-spline curve interpolation to point data, Computer-Aided Design, 33, 2001, 967-974. DOI: 10.1016/S0010-4485(00)00133-0
[24] Piegl, L.A.; Tiller, W.: The NURBS Book, Springer-Verlag, Berlin, 1997, 179-188.
[25] Shiba, R.; Sorbie, C.; Siu, D.-W.; Bryant, J.-T.; Cooke, T.-D. V.; Wevers, H.-W.: Geometry of the Humeroulnar Joint, Journal of Orthopaedic Research, 6, 1988, 897-906.
[26] Stokdijk, M.; Meskers, C.G.M.; Veeger, H.E.J.; de Boer, Y.A.; Rozing, P.M.: Determination of the optimal elbow axis for evaluation of placement of prostheses, Clinical Biomechanics, 14, 1999, 177-184. DOI: 10.1016/S0268-0033(98)00057-6
[27] Schroeder, W.; Martin, K.; and Lorensen, B.: The Visualization Toolkit, 2006, Kitware.
[28] Tutunea-Fatan, O.R; Bernick, J.H; Lalone, E.; King, G.J.W.; Johnson, J.A.: Application of collision detection to assess implant insertion in elbow replacement surgery. In: Proceedings of SPIE, 7625, 2010, 7625K1-12. DOI: 10.1117/12.840548.